Tuning Electronic Transport in a Self-Assembled Nanocomposite

Wei Sea Chang,[†] Heng-Jui Liu,[†] Vu Thanh Tra,[‡] Jhih-Wei Chen,[§] Tzu-Chiao Wei,[⊥] W. Y. Tzeng,[∥] Yuanmin Zhu,[⊗] Ho-Hung Kuo,[†] Ying-Hui Hsieh,[†] Jheng-Cyuan Lin,[◇] Qian Zhan,[⊗] Chih Wei Luo,[∥] Jiunn-Yuan Lin,[‡] Jr-Hau He,[⊥] Chung Lin Wu,[§] and Ying-Hao Chu[†,*]

[†]Department of Materials Science and Engineering, National Chiao Tung University, Hsinchu 30010, Taiwan, [‡]Institute of Physics, National Chiao Tung University, Hsinchu 30010, Taiwan, [§]Department of Physics, National Cheng Kung University, Tainan 70101, Taiwan, [⊥]Institute of Photonics and Optoelectronics and Department of Electrical Engineering, National Taiwan University, Taipei 10617, Taiwan, [∥]Department of Electrophysics, National Chiao Tung University, Hsinchu 30010, Taiwan, [⊗]Department of Material Physics and Chemistry, University of Science and Technology Beijing, Beijing 100083, China, and [◇]Institute of Physics, Academia Sinica, 128 Sec. 2, Academia Road, Nankang, Taipei, 11529, Taiwan

ABSTRACT Self-assembled nanocomposites with a high interface-to-volume ratio offer an opportunity to overcome limitations in current technology, where intriguing transport behaviors can be tailored by the choice of proper interactions of constituents. Here we integrated metallic perovskite oxide $SrRuO_3$—wurzite semiconductor ZnO nanocomposites to investigate the room-temperature metal—insulator transition and its effect on photoresponse. We demonstrate that the band structure at the interface can be tuned by controlling the interface-to-volume ratio of the nanocomposites. Photoinduced carrier injection driven by visible light was detected across the nanocomposites. This work shows the charge interaction of the vertically integrated multiheterostructures by incorporating a controllable interface-to-volume ratio, which is essential for optimization of the design and functionality of electronic devices.

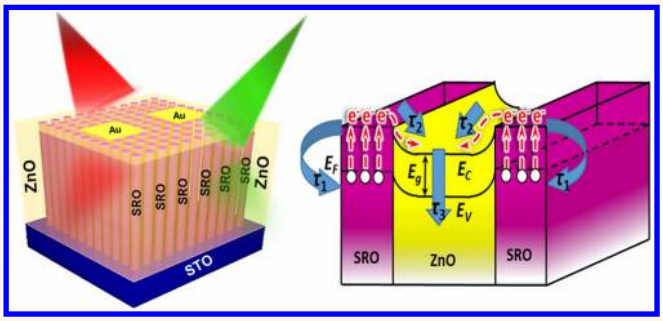

KEYWORDS: metal—insulator transition · interface-to-volume ratio · band diagram · self-assembled · nanocomposites

When two oxide materials with a difference in band-gap energies is accommodated, the interfacial properties depend on how the oxide interfaces make contact with each other. Often, the interplay between spin, lattice, orbit, and charge at the oxide interfaces offers novel electronic properties that are not attainable in conventional semiconductors.[1−6] With recent advances in growth and *in situ* characterization, controllable interface quality at the atomic level has led to a breakthrough, allowing the possibility to design flexible devices with advanced functionality.[7,8] Prominent examples are self-assembled nanocomposites exhibiting strong and controllable magnetoelectric coupling in combination with piezoelectric perovskites—ferrimagnetic spinels (*i.e.*, $BaTiO_3$—$CoFe_2O_4$,[9] $BiFeO_3$—$CoFe_2O_4$,[10,11] *etc.*), abnormal dielectric response in $BiFeO_3$—Sm_2O_3,[12] and enhanced ferroelectricity in $BaTiO_3$—Sm_2O_3.[13] Intriguing transport behaviors have been shown including enhanced critical current in superconductors[14] and low-magnetic-field-driven colossal magnetoresistance in manganite[15,16] and non-manganite[17]-based systems.

Our approach is to take advantage of the high interface-to-volume ratio in self-assembled nanocomposites[18−21] to create multiple interface junctions to manipulate the charge interaction through vertically integrated multiheterostructures. This type of nanocomposites could find applications in large electronic devices due to the coupling of photon degrees of freedom based on the charge interaction in the multiple interfaces and decoupling of the phonon and electrical conductions. Although the scattering of phonons and electrons is enhanced through the nanocomposite design, the electrical conduction can be enhanced by varying the amount of interface junction to decouple phonon and electrical conduction.[22,23]

* Address correspondence to yhc@nctu.edu.tw.

Received for review March 27, 2014 and accepted May 19, 2014.

Published online May 19, 2014
10.1021/nn501682t

In this study, we chose a $SrRuO_3$ (SRO)−ZnO self-assembled nanocomposite as a model system to show a systematic way to engineer the conducting behaviors in the heterostructures. SRO is a well-known metal oxide and has served as a bottom electrode in oxide-based electronics.[24] ZnO, on the other hand, is a well-known wide-band semiconductor with various intriguing functionalities.[25,26] In such a nanocomposite, the electron transport behavior can be tuned from an insulator to a metal mediated by interface-to-volume ratio in the SRO−ZnO heterostructure. The origin of this is the charge interaction at the interface revealed by a combination of X-ray photoelectron spectroscopy (XPS), ultrafast dynamics, and photoconduction. Such a result delivers a generic design rule to engineer the conduction of self-assembled nanocomposites and offer new solutions in spintronic, optoelectronic, and thermoelectric applications.

RESULTS AND DISCUSSION

Self-assembled SRO−ZnO nanocomposites were grown on a STO(111) single-crystal substrate by using pulsed laser deposition (PLD) as described in the Methods section.[17] The growth of the SRO−ZnO nanostructures was monitored *in situ* using RHEED. At the initial growth stage, the RHEED pattern transformed gradually from streaks to spots after the first few sequential deposition cycles from the SRO−ZnO dual target, indicating that the streaky pattern of the STO substrate has been covered with SRO and ZnO islands. Continuing the SRO−ZnO sequential deposition, the streaks eventually disappear with increased intensity of the specular spot. This implies that island formation took place during growth as the RHEED pattern evolves into a symmetric spotty pattern. Figure 1a shows the RHEED pattern taken along the in-plane [11$\bar{2}$] direction of STO at the end of growth. The spotty pattern is observed at every 60° azimuthal rotation. The simulated feature demonstrates a good agreement with the observed RHEED pattern. The pattern is assigned to ZnO(002) and three sets of SRO(110) domain variants corresponding to 0°, 60°, and 120°. In order to gain more structural insights, high-resolution XRD has been employed. Figure 1b shows a typical X-ray diffraction (XRD) $\theta-2\theta$ scan of the SRO−ZnO system. Only the SRO(110) series of peaks and ZnO(002) series of peaks were detected in the vicinity of the STO substrate, implying well-aligned SRO and ZnO along the out-of-plane direction. These pronounced peaks show a clear phase separation of SRO and ZnO, with the out-of-plane lattice constants calculated as 2.771 and 5.214 Å. Furthermore, ϕ-scanning was employed to analyze the in-plane relation, as shown in Figure 1c. Six ZnO(110) peaks of the stronger set were observed at 60° intervals, confirming that the epitaxial ZnO has a predominant single domain with hexagonal symmetry. Meanwhile, the observation of six SRO(002) peaks at 60° intervals is ascribed to the coexistence of three SRO(110) domain variants in-plane, consistent with that determined from the RHEED patterns. A high-resolution in-plane reciprocal space map (HR-RSM) was obtained to measure the epitaxial relation of the system (Figure 1d). The HR-RSM reveals the in-plane epitaxial relation as SRO⟨002⟩ || ZnO⟨110⟩ || STO⟨11$\bar{2}$⟩, which is in excellent agreement with the results from RHEED and ϕ-scanning.

Further microstructure identification of SRO−ZnO nanocomposites was carried out by transmission electron microscopy (TEM). Figure 2a−d show the cross-sectional TEM images. In Figure 2a, both SRO and ZnO

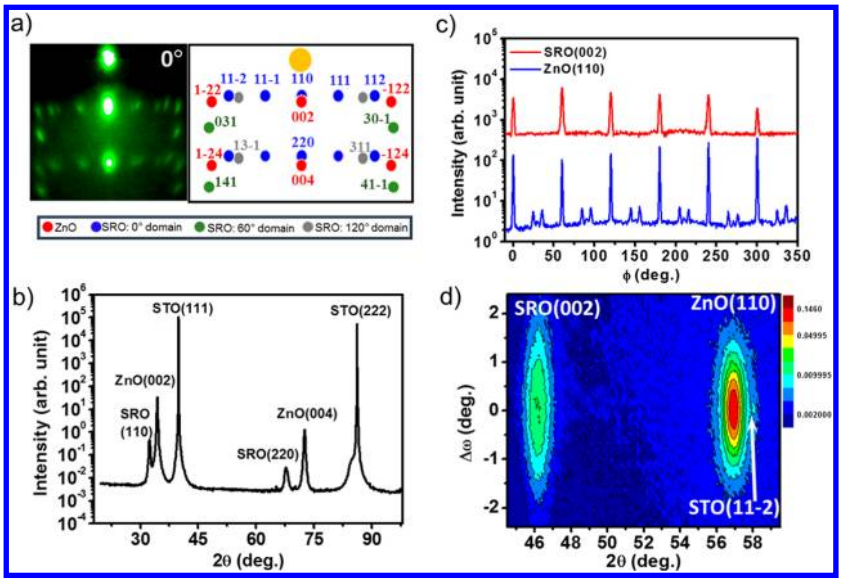

Figure 1. (a) RHEED pattern taken along the [11$\bar{2}$] STO substrate and the corresponding simulated pattern. (b) XRD $\theta-2\theta$ scans around the STO(111) series of peaks. (c) In-plane epitaxial structure revealed by XRD ϕ-scans of SRO(002) and ZnO(110). (d) In-plane HR-RSM scan around the [11$\bar{2}$] STO substrate.

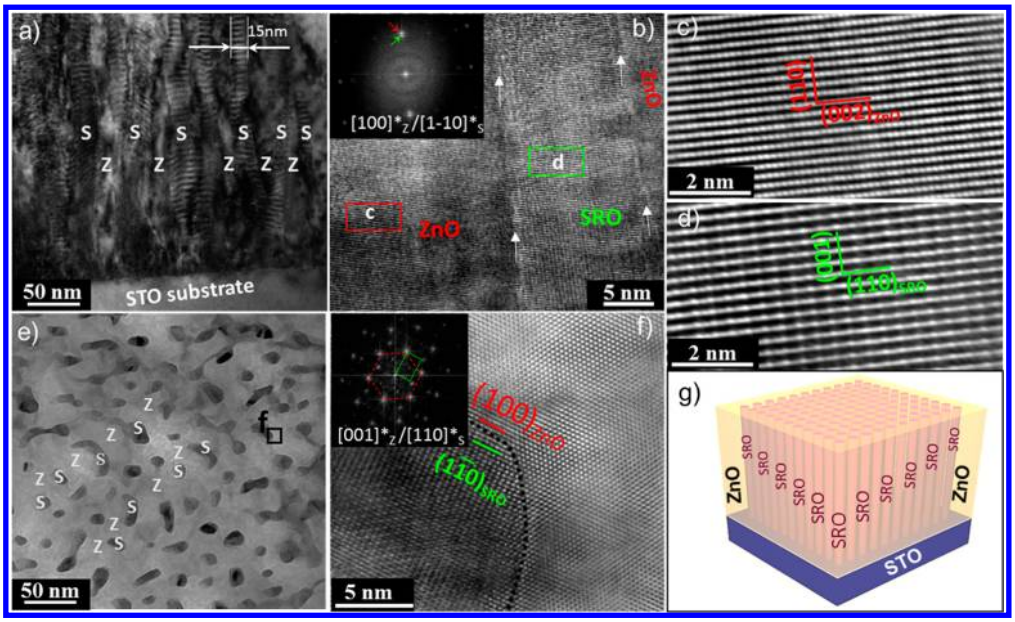

Figure 2. (a) Cross-sectional TEM image of SRO−ZnO on a STO substrate. "S" represents the SRO phase and "Z" is the ZnO phase. (b) HR-TEM cross section image of the SRO−ZnO interface and the corresponding FFT pattern in the inset. Enlarged TEM images taken from the area labeled as the (c) ZnO region and (d) SRO region with the major planes marked. (e) Plan-view TEM image of SRO−ZnO with (f) zoom-in HR-TEM image and the corresponding FFT pattern as an inset and (g) schematic representations of a self-assembled SRO−ZnO heterostructure.

phases show a vertically aligned columnar structure with SRO columns at an average width of ∼15 nm, indicating that the SRO−ZnO systems are self-assembled. The two phases have grown alternately on the STO substrate. A high-resolution TEM (HR-TEM) image of the interface between ZnO and SRO as indicated by the arrows is shown in Figure 2b, with the fast Fourier transform (FFT) diffraction pattern in the inset. Figure 2c−d exhibit the zoom-in HR-TEM images of the marked area in ZnO and SRO, respectively. The epitaxial relationships between the two layers are ZnO(110) || SRO(001) and ZnO(002) || SRO(110). Plan-view TEM images in Figure 2e, f taken along the zone axis of $[001]_{ZnO}//[110]_{SRO}$ show the surface morphology of the SRO−ZnO system. Figure 2f exhibits the selected area for zoom-in HR-TEM of the interface between ZnO and SRO, having an in-plane orientation relationship of ZnO(100) || SRO($1\bar{1}0$). The inset of Figure 2f shows the FFT pattern from the same region, confirming that the ZnO wurtzite hexagonal structure is a matrix and SRO perovskites are nanopillars. One should note that HR-TEM images in Figure 2b and f show a sharp and well-defined interface between the ZnO matrix and SRO nanostructure. The clear FFT patterns in the corresponding insets also demonstrate the obvious phase separation. TEM results corroborated by RHEED and XRD measurements exhibited a 3-D orientation relationship of SRO($1\bar{1}0$)(002)[110] || ZnO(100)(110)[001] || SRO(110)($11\bar{2}$)[111]. A model demonstrating 3-D heteroepitaxial self-assembled SRO−ZnO nanostructures with a high-quality interface is proposed in Figure 2g, in which SRO(110) nanopillars are embedded in the (002)-oriented ZnO matrix.

We explore the charge carrier dynamics of the self-assembled SRO−ZnO vertical nanocomposites mediated by a high interface-to-volume ratio. Figure 3a shows the Zn 3s and Sr 3d core levels of the SRO−ZnO heterostructures. The Zn 3s core level reveals no binding energy shift, while the Sr 3d core level shifts about 0.20 eV when V_{SRO} increased from 29% to 40%. The core-level energy separation ΔE_{CL} between the Zn 3s and Sr 3d is determined as 8.0 and 7.8 eV with respect to V_{SRO} = 29% and 40%. By combining the valence band maximum (VBM) with the core-level value from the bare ZnO and SRO epilayers, within the heterostructure system, the apparent valence band offset (VBO) values of V_{SRO} = 29% and 40% are 3.41 and 3.21 eV, respectively. This result shows a significant decrement of 0.20 eV at the VBO with increased V_{SRO}. The equilibrium energy band diagrams of the SRO−ZnO heterostructures of different amounts of SRO nanopillars are illustrated in Figure 3b−d. In the crystalline ZnO interfaces, the electrons from interfacial trap states and/or defects would cause the electrons to become depleted inside the semiconductor materials, resulting in band bending near the interfaces,[27−30] and would thus modulate the electronic conduction.[31−34] As the SRO to ZnO ratio changes, the vertical heterostructures designed with low V_{SRO} are partially depleted due to the smaller depletion region (∼20 nm) than the average spacing between SRO nanopillars of about ∼80 nm (Figure 3b). The SRO−ZnO with high V_{SRO} are, however, completely depleted when the depletion region is equal to or greater than the average spacing between SRO nanopillars of about ∼20 nm (Figure 3c,d). In the band diagram with a denser

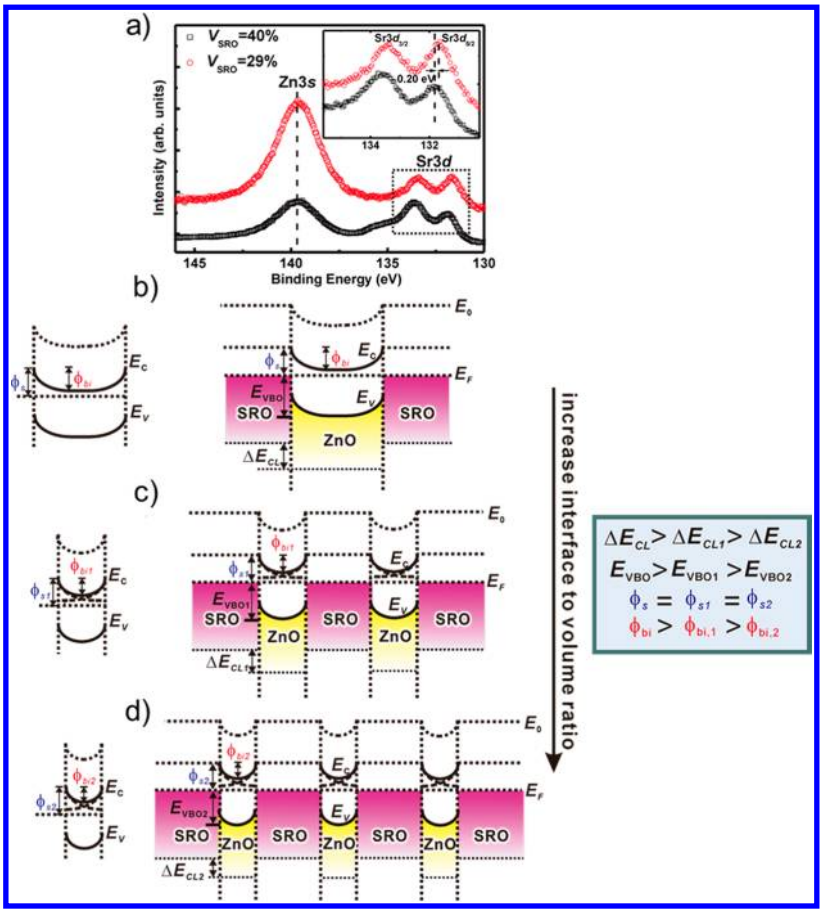

Figure 3. Equilibrium energy band diagrams with (a) the Zn 3s and Sr 3d core-level characterization of V_{SRO} = 29% and 40% with the corresponding core-level energy separation ΔE_{CL} between the Zn 3s and Sr 3d in the inset. (b–d) Schematic band diagrams of the SRO–ZnO heterostructures mediated by the interface-to-volume ratio resulting from increasing the SRO nanopillars, where E_F is the Fermi level, E_C is the conduction band minima, E_V is the valence band maxima, E_{VBO} is the valence band offset, ϕ_{bi} is the surface band bending, and ϕ_s is the surface potential.

SRO, the Sr 3d core level is shifted toward the band edge, which is thus related directly to the ΔE_{CL}. Accordingly, the VBO of the SRO–ZnO heterostructures is shown to decrease at higher V_{SRO} as a result of a lower surface band bending ϕ_{bi} appearing in the ZnO. Thus, under the specifically applied bias, thermally excited electrons can easily overcome the lower surface band bending ϕ_{bi} to give rise to high electrical conductivity. This model based on V_{SRO}-derived electronic structure modification is in good agreement with previously reported ZnO nanowire studies.[28,35,36]

The electron transport measurements and conductive atomic force microscopy (C-AFM) are shown in Figure 4. We observed an increase in the number of SRO nanopillars with increasing SRO volume fraction, V_{SRO}; for example, the image sequence in Figure 4a obtained from C-AFM shows distinct differences in the number of SRO nanopillars between samples with respect to V_{SRO}. Each of the nanopillars is conductive. The average spacing between the nanopillars decreases in each development step until they are too close to each other (V_{SRO} = 75%). To understand the conduction process at room temperature, the electron

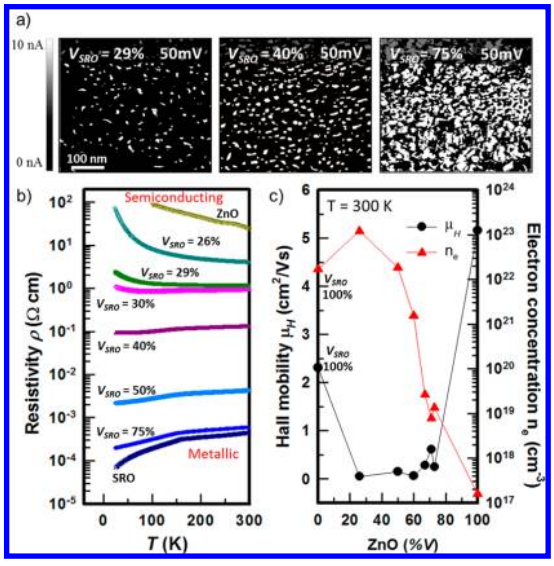

Figure 4. (a) C-AFM images taken with a sample bias of 50 mV applied to the sample surface. (b) Temperature dependence of the resistivity for the SRO–ZnO heterostructures with different V_{SRO} showing clearly the semiconductor-to-metal transition. (c) Room-temperature Hall mobility and carrier concentration.

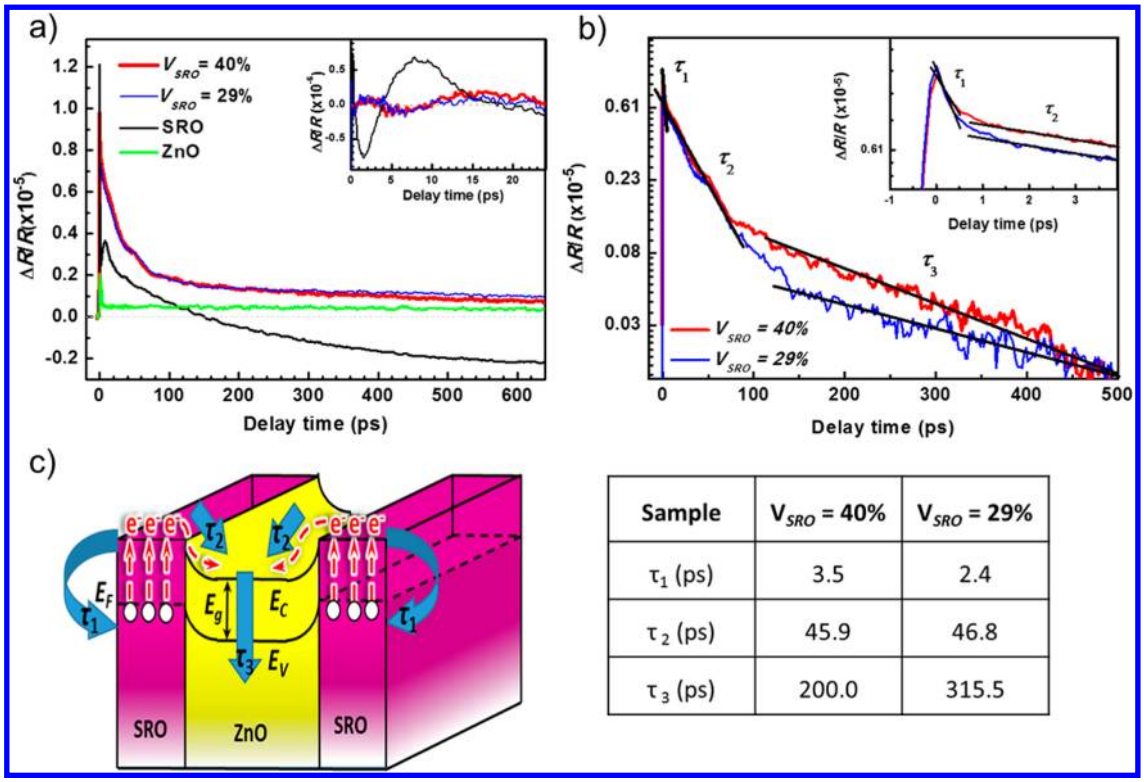

Sample	V_{SRO} = 40%	V_{SRO} = 29%
τ_1 (ps)	3.5	2.4
τ_2 (ps)	45.9	46.8
τ_3 (ps)	200.0	315.5

Figure 5. (a) Typical $\Delta R/R$ curves in the samples of SRO−ZnO, SRO, and ZnO. Inset: Oscillation component extracted from the $\Delta R/R$ curves. (b) $\Delta R/R$ curves of SRO−ZnO in (a) presented in a semilogarithmic scale. The inset shows a part of (b) close to zero delay time. (c) Schematic electronic band structure of SRO−ZnO and the relaxation processes of photoexcited carriers. Table on the right shows the respective relaxation times.

paths of the composition range V_{SRO} 75%, 50%, 40%, 30%, 29%, and 26% were measured by means of four-point probe resistivity measurement. Figure 4b presents the resistivity ρ of SRO−ZnO with different V_{SRO} compared to the resistivity of pure SRO and ZnO thin films as a function of temperature. Pure SRO exhibits metallic behavior with a positive resistivity−temperature slope ($d\rho/dT > 0$). A kink at $T_c \approx 160$ K is due to reduced magnetic scattering below the Curie temperature.[24] The resistivity of pure ZnO is seen to increase monotonically with decreasing temperature throughout the entire measured temperature. It is seen in this figure, by bringing the SRO and ZnO together, the SRO−ZnO heterostructures demonstrate a room-temperature resistivity of 1 to 4 orders of magnitude lower than that of pure ZnO film, suggesting that the conductivity of SRO−ZnO heterostructures can be tuned from semiconducting to metallic. The behavior of SRO−ZnO heterostructures with respect to interface-to-volume ratio does indeed indicate significant change in the electron transport behavior. The Hall measurements (Figure 4d) were carried out to determine the carrier concentration (n_e) and Hall mobility (μ_H) of the respective SRO−ZnO heterostructures at room temperature. We observed an increasing carrier concentration from $\sim 10^{17}$ to $\sim 10^{23}$ cm^{-3} with increasing SRO volume fraction despite a subsequent decrease in the mobility. The relationship between resistivity, carrier concentration, and Hall mobility in the SRO−ZnO system can be deduced from $\rho = 1/qn_e\mu_H$ where q is the electric charge. One cause of the low mobility could be due to the several scattering mechanisms limiting the mobility at the different carrier concentrations.

Figure 5a shows the photoinduced $\Delta R/R$ in the SRO−ZnO heterostructure. Electronic excitations generated by the pump pulses in SRO nanopillars result in a swift rise of $\Delta R/R$ at zero delay time. These photoexcited electrons inside SRO nanopillars further decay *via* three processes, as shown in Figure 5c, which can be clearly identified by the three different slopes (three relaxation processes) in the $\Delta R/R$ of Figure 5b. Process I: The high-energy photoexcited electrons inside the SRO nanopillars will release their energy through the scattering with longitudinal-optical phonons and travel to the boundary between ZnO and SRO within several picoseconds (τ_1 in Figure 5b). This process is consistent with the fast relaxation component of a pure SRO thin film in Figure 5a. Process II: The high-energy photoexcited electrons inside SRO nanopillars transfer into the ZnO matrix; that is, the photoexcited electrons pass through the boundary between ZnO and SRO in several tens of picosecond (τ_2 in Figure 5b). Additionally, the $\Delta R/R$ displays an oscillated feature, which is also observed in a pure SRO thin film. For the case of pure SRO, the pump pulse induces an electronic

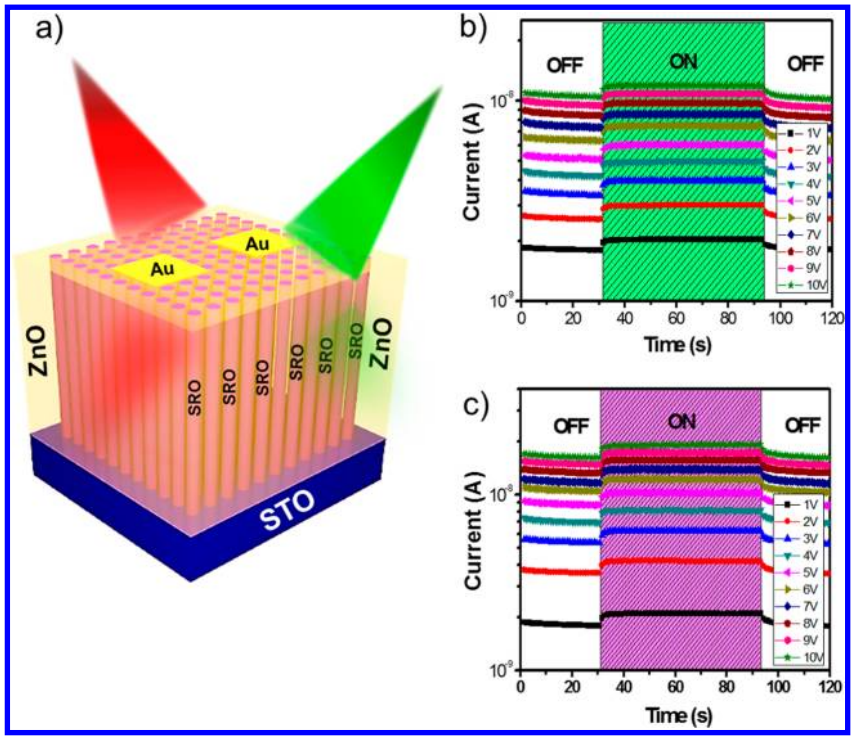

Figure 6. (a) Schematic illustration of the SRO–ZnO heterostructure by green (532 nm) and red (633 nm) laser illumination. Photocurrent as a function of time under (b) 532 nm and (c) 633 nm laser illumination with a light intensity of 10^4 W/m^2. The photocurrent increased with the bias between 1 and 10 V and became saturated to the "flatband" voltage, *i.e.*, ~10 V.

excitation that generates a mechanical stress of the lattice *via* the coupling of the electronic system to lattice degrees of freedom.[37] However, the characteristics (amplitude and phase) of the oscillation components are significantly different, as shown in the inset of Figure 5a. It implies that the oscillation signals in the SRO–ZnO heterostructure are mainly from the ZnO matrix rather than the SRO nanopillars. While the photoexcited electrons diffuse from SRO nanopillars into the ZnO matrix, the excited electrons accumulate at the boundary between the SRO nanopillars and ZnO matrix to change the band-bending effect in ZnO. According to the piezoelectric properties of ZnO,[38] the variations of the built-in electric field from the changes of the band-bending effect will further cause the contraction (or expansion) of the lattice to generate the strain pulses inside ZnO and then induce the oscillation signal in $\Delta R/R$. This strongly indicates that the photoexcited electrons in SRO indeed transfer into the ZnO. Process III: The high-energy photoexcited electrons inside the ZnO matrix further release their energy in several hundreds of picoseconds (τ_3 in Figure 5b), which is attributed to the relaxation of the band-filling effect, dominated by nonradiative carrier recombinations within the defect states caused by the Zn and O vacancies or impurities in ZnO.[39] The time scale of this process is consistent with the $\Delta R/R$ of a pure ZnO film in Figure 5a. For the fast component in $\Delta R/R$, the relaxation time τ_1 of V_{SRO} = 40% and 29% is 3.5 and 2.4 ps (obtained by fitting the $\Delta R/R$ curves in Figure 5b), respectively. Due to the larger percentage of ZnO in an SRO–ZnO heterostructure of V_{SRO} = 29%, more photoexcited electrons in SRO nanopillars would transfer into the ZnO matrix to shorten the relaxation time τ_1 of photoexcited electrons in SRO nanopillars. On the other hand, more photoexcited electrons inside the ZnO matrix and a larger percentage of ZnO, which is a kind of trapping center, would further cause longer relaxation time τ_3. Consequently, the τ_3 of 315.5 ps for V_{SRO} = 29% is larger than that of 200.0 ps for V_{SRO} = 40%. Moreover, the relaxation time τ_2 for both V_{SRO} = 40% and 29% is, respectively, 45.9 and 46.8 ps. This indicates that the τ_2 of carriers passing through the boundary between ZnO and SRO is independent of the ratio between SRO and ZnO.

We further investigated the photoresponse of SRO–ZnO nanocomposites (V_{SRO} = 29%) using continuous wave photoexcitation with two visible light wavelengths corresponding to green (532 nm) and red (633 nm) colors. A schematic diagram representing the system is shown in Figure 6a. The photocurrent as a function of time at different bias conditions upon visible light illumination is shown in Figure 6b,c. As seen, the current increased when the samples were illuminated by visible light (ON state) and recovered back to its original state when the light was off (OFF state). These observations suggest that photoexcitation of the SRO nanopillars in the visible light yields electrons to transport over the Schottky barrier into

ZnO matrix. We chose visible light because of the strong visible light absorption in SRO,[40] in which the photoresponse can be correlated to the spectral behavior of the SRO nanopillars across the visible spectrum rather than the absorption of the ZnO matrix with the band-gap of 3.37 eV. Transport of these free electrons results in a photocurrent with a simultaneous increase in electrical conductivity. Therefore, the SRO–ZnO nanocomposites could be used as visible light photodetectors, which is not achievable with the photodetectors consisting of pure ZnO and thus extends the application of ZnO-based UV photodetectors.[41] Briefly, the observed results can be elucidated by the electronic excitation in SRO with a longer relaxation time τ_3, as pointed out in ultrafast pump–probe spectroscopy. In the metallic sample, despite having more SRO nanopillars, the ZnO width becomes narrower (interspacing between SRO nanopillars becomes smaller). Under this circumstance, only a negligible amount of the electrons will contribute to photoconduction.

CONCLUSION

In summary, we have demonstrated that the self-assembled SRO–ZnO nanocomposite with high interface-to-volume ratio can be used to tune and control the electron transport behavior. This effect is enabled by engineering the Schottky barrier and band alignment by varying the interface-to-volume ratio of the SRO–ZnO heterostructure. Ultrafast dynamics and photoresponsivity were studied in visible light to observe the light absorption of the trapped SRO electrons in a ZnO matrix. This provides important insight into the working principle of the room-temperature metal–insulator transition and consequently the capability to modify and manipulate the electronic properties, which may become important for the design of new functional electronic devices.

METHODS

Self-assembled SRO–ZnO nanocomposites were grown on a (111)-oriented single-crystal STO substrate at 800 °C using dual targets (SRO and ZnO). Pulse laser deposition with a KrF excimer laser (λ = 248 nm, Lambda Physik) was operated at 10 Hz laser repetition rate in an oxygen atmosphere of 100 mTorr. The ZnO and SRO targets were mounted on a computer-controlled rotation stage to allow laser pulses to hit the respective deposition surface targets alternatively; for instance, after every *x* number of pulses on the ZnO target, the SRO target was set into position, and a number of *y* pulses were applied. This was repeated *p* times. By using a sequential dual-target deposition process, it offers the flexibility to manipulate the composition of oxide thin films by adjusting the number of laser pulses on each deposition target. The change in the volume fraction of SRO and ZnO is thereby achieved by changing the number of laser pulses. The total thickness of the SRO–ZnO system was kept constant at 250 nm. The growth rates for ZnO and SRO are about 0.2 and 0.1 Å per pulse, respectively.

The femtosecond spectroscopy measurement was performed using a commercial Ti:sapphire laser (repetition rate: 5.2 MHz, wavelength: 800 nm, pulse duration: 70 fs) and a homemade dual-color pump–probe system with the standard lock-in technique at room temperature. The power of the pump beam and the probe beam are 10 and 1 mW, respectively. The pump pulses have a corresponding photon energy (3.1 eV) below the band-gap of ZnO (3.37 eV), which cannot excite carriers in the ZnO matrix and, hence, can generate electronic excitations only inside the SRO nanopillars. Excitation dynamics is studied by measuring the photoinduced transient reflectivity changes ($\Delta R/R$) of the probe beam with photon energy of 1.55 eV.

For photoresponsivity measurement, 200 μm by 200 μm and 100 nm thick Ti/Au square electrodes were deposited by electron-beam evaporation. The space between each electrodes is 200 μm. The Keithley 4200-SCS semiconductor characterization system was used to measure *I*–*V* characteristics and responsivity of the SRO–ZnO vertical nanostructures, and the time-resolved measurement was assisted by a mechanical shutter to modulate the frequency of light. For these measurements, the power intensity of the 532 and 633 nm lasers (beam diameter is ~1 mm) is 10^4 W/m^2. To compare the photoresponse of 532 and 633 nm, the same illumination time of 90 s was used.

Conflict of Interest: The authors declare no competing financial interest.

Acknowledgment. This work is supported by the National Science Council, R.O.C. (NSC-101-2119-M-009-003-MY2), Ministry of Education (MOE-ATU 101W961), Center for Interdisciplinary Science of National Chiao Tung University, and National Natural Science Foundation of China with Grant Nos. 51371031 and 50971015.

Supporting Information Available: Additional data and text are described in the Supporting Information. This material is available free of charge *via* the Internet at http://pubs.acs.org.

REFERENCES AND NOTES

1. Hwang, H. Y.; Iwasa, I.; Kawasaki, M.; Keimer, B.; Nagaosa, N.; Tokura, T. Emergent Phenomena at Oxide Interfaces. *Nat. Mater.* **2012**, *11*, 103–113.
2. Takagi, H.; Hwang, H. Y. An Emergent Change of Phase for Electronics. *Science* **2010**, *327*, 1601–1602.
3. Ohtomo, A.; Hwang, H. Y. A High-Mobility Electron Gas at the $LaAlO_3/SrTiO_3$ Heterointerface. *Nature* **2004**, *427*, 423–426.
4. Okamoto, S.; Millis, A. J. Electronic Reconstruction at an Interface between a Mott Insulator and a Band Insulator. *Nature* **2004**, *428*, 630–633.
5. Dagotto, E. When Oxides Meet Face to Face. *Science* **2007**, *318*, 1076–1077.
6. Jang, H. W.; Felker, D. A.; Bark, C. W.; Wang, Y.; Niranjam, M. K.; Nelson, C. T.; Zhang, Y.; Su, D.; Folkman, C. M.; Baek, S. H.; *et al.* Metallic and Insulating Oxide Interfaces Controlled by Electronic Correlations. *Science* **2011**, *331*, 886–889.
7. Schlom, D. G.; Chen, L. Q.; Pan, X.; Schmehl, A.; Zurbuchen, M. A. A Thin Film Approach to Engineering Functionality into Oxides. *J. Am. Ceram. Soc.* **2008**, *91*, 2429–2454.
8. Martin, L. W.; Chu, Y. H.; Ramesh, R. Advances in the Growth and Characterization of Magnetic, Ferroelectric, and Multiferroic Oxide Thin Films. *Mater. Sci. Eng., R* **2010**, *68*, 89–133.
9. Zheng, H.; Wang, J.; Lofland, S. E.; Ma, Z.; Mohaddes-Ardabili, L.; Zhao, T.; Salamanca-Riba, L.; Shinde, S. R.; Ogale, S. B.; Bai, F.; *et al.* Multiferroic $BaTiO_3$-$CoFe_2O_4$ Nanostructures. *Science* **2004**, *303*, 661–663.
10. Zavaliche, F.; Zheng, H.; Mohaddes-Ardabili, L.; Yang, S. Y.; Zhan, Q.; Shafer, P.; Reilly, E.; Chopdekar, R.; Jia, Y.; Wright, P.; *et al.* Electric Field-Induced Magnetization Switching in Epitaxial Columnar Nanostructures. *Nano Lett.* **2005**, *5*, 1793–1796.

11. Zavaliche, F.; Zhao, T.; Zheng, H.; Straub, F.; Cruz, M. P.; Yang, P.-L.; Hao, D.; Ramesh, R. Electrically Assisted Magnetic Recording in Multiferroic Nanostructures. *Nano Lett.* **2007**, *7*, 1586–1590.
12. Yang, H.; Wang, H.; Yoon, J.; Wang, Y.; Jain, M.; Feldmann, D. M.; Dowden, P. C.; Judith, L.; Jia, Q. Vertical Interface Effect on the Physical Properties of Self-Assembled Nanocomposite Epitaxial Films. *Adv. Mater.* **2009**, *21*, 3794–3798.
13. Harrington, S. A.; Zhai, J.; Denev, S.; Gopalan, V.; Wang, H.; Bi, Z.; Redfern, S. A. T.; Baek, S.-H.; Bark, C. W.; Eom, C.-B.; *et al*. Thick Lead-Free Ferroelectric Films with High Curie Temperatures through Nanocomposite-Induced Strain. *Nat. Nanotechnol.* **2011**, *6*, 491–195.
14. Reyren, N.; Thiel, S.; Caviglia, A. D.; Fitting Kourkoutis, L.; Hammert, G.; Richter, C.; Schneider, C. W.; Kopp, T.; Ruetschi, A.-S.; Jaccard, D.; *et al*. Superconducting Interfaces between Insulating Oxides. *Science* **2007**, *317*, 1196.
15. Chen, A. P.; Bi, Z.; Tsai, C.-F.; Lee, J. W.; Su, Q.; Zhang, X.; Zhang, X.; Jia, Q.; MacManus-Driscoll, J. L.; Wang, H. Tunable Low-Field Magnetoresistance in $(La_{0.7}Sr_{0.3}MnO_3)_{0.5}$:$(ZnO)_{0.5}$ Self-Assembled Vertically Aligned Nanocomposite Thin Films. *Adv. Funct. Mater.* **2011**, *21*, 2423–2429.
16. Kang, B. S.; Wang, H.; MacManus-Driscoll, J. L.; Li, Y.; Jia, Q. X. Low Field Magnetotransport Properties of $(La_{0.7}Sr_{0.3}MnO_3)_{0.5}$:$(ZnO)_{0.5}$ Nanocomposite Films. *Appl. Phys. Lett.* **2006**, *88*, 192514.
17. Liu, H.-J.; Tra, V.-T.; Chen, Y.-J.; Huang, R.; Duan, C.-G.; Hsieh, Y.-H.; Lin, H.-J.; Lin, J.-Y.; Chen, C.-T.; Ikuhara, Y.; *et al*. Large Magnetoresistance in Magnetically Coupled $SrRuO_3$-$CoFe_2O_4$ Self-Assembled Nanostructures. *Adv. Mater.* **2013**, *25*, 4753–4759.
18. Nan, C. W.; Bichurin, M. I.; Dong, S.; Viehalnd, D.; Srinivasan, G. Multiferroic Magnetoelectric Composites: Historical Perspective, Status, and Future Directions. *J. Appl. Phys.* **2008**, *103*, 031101.
19. MacManus-Driscoll, J. L. Self-Assembled Heteroepitaxial Oxide Nanocomposite Thin Film Structures: Designing Interface-Induced Functionality in Electronic Materials. *Adv. Funct. Mater.* **2010**, *20*, 2035–2045.
20. Liu, H.-J.; L.-Y; He, Q.; Liang, C.-W.; Chen, Y.-Z.; Chien, Y.-S.; Hsieh, Y.-H.; Lin, S.-J.; Arenholz, E.; Luo, C.-W.; *et al*. Epitaxial Photostriction-Magnetostriction Coupled Self-Assembled Nanostructures. *ACS Nano* **2012**, *6*, 6952–6959.
21. Chen, Y.-J.; Hsieh, Y.-H.; Liao, S.-C.; Hu, Z.; Huang, M.-J.; Kuo, W.-C.; Chin, Y.-Y; Uen, T.-M.; Juang, J.-Y.; Lai, C.-H.; *et al*. Strong Magnetic Enhancement in Self-Assembled Multiferroic-Ferrimagnetic Nanostructures. *Nanoscale* **2013**, *5*, 4449–4453.
22. Snyder, G. J.; Toberer, E. S. Complex Thermoelectric Materials. *Nat. Mater.* **2008**, *7*, 105–114.
23. Li, J.-F.; Liu, W.-S.; Zhao, L.-D.; Zhou, M. High Performance Nanostructured Thermoelectric Materials. *NPG Asia Mater.* **2010**, *2*, 152–158.
24. Koster, G.; Klein, L.; Siemons, W.; Rijnders, G.; Dodge, J. S.; Eom, C.-B.; Blank, D. H. A.; Beasley, M. R. Structure, Physical Properties, and Applications of $SrRuO_3$ Thin Films. *Rev. Mod. Phys.* **2012**, *84*, 253–298.
25. Chen, C. Y.; Chen, M. W.; Ke, J. J.; Lin, C. A.; Retamal, J. R. D.; He, J. H. Surface Effects on Optical and Electrical Properties of ZnO Nanostructures. *Pure Appl. Chem.* **2010**, *82*, 2055–2073.
26. Janotti, A.; Van de Walle, C. G. Fundamentals of Zinc Oxide as a Semiconductor. *Rep. Prog. Phys.* **2009**, *72*, 126501.
27. Liao, Z. M.; Liu, K.-J.; Zhang, J.-M.; Xu, J.; Yu, D.-P. Effect of Surface States on Electron Transport in Individual ZnO Nanowires. *Phys. Lett. A* **2007**, *367*, 207–210.
28. Chen, C. Y.; Retamal, J. R. D.; Wu, I.-W.; Lien, D.-H.; Chen, M.-W.; Dingm, Y.; Chueh, Y.-L.; Wu, C.-I; He, J.-H. Probing Surface Band Bending of Surface-Engineered Metal Oxide Nanowires. *ACS Nano* **2012**, *6*, 9366–9372.
29. Ivan, M. S.; Fabregat-Santiago, F.; Denier, B.; Bisquert, J.; Tena-Zaera, R.; Elias, J.; Levy-Clement, C. Determination of Carrier Density of ZnO Nanowires by Electrochemical Techniques. *Appl. Phys. Lett.* **2006**, *89*, 203117.
30. Andrei, K.; Martin, M. Chemical Sensing and Catalysis by One-Dimensional Metal-Oxide Nanostructures. *Annu. Rev. Mater. Res.* **2004**, *34*, 151–180.
31. Ju, S.; Lee, K.; Yoon, M.-H.; Facchetti, A.; Marks, T. J.; Janes, D. B. High Performance ZnO Nanowire Field Effect Transistors with Organic Gate Nanodielectrics: Effects of Metal Contacts and Ozone Treatment. *Nanotechnology* **2007**, *18*, 155201.
32. Fan, Z.; Wang, D.; Chang, P.-C.; Tseng, W.-Y.; Lu, J. G. ZnO Nanowire Field-Effect Transistor and Oxygen Property. *Appl. Phys. Lett.* **2004**, *85*, 5923.
33. Hossain, F. M.; Nishii, J.; Takagi, S.; Ohtomo, A.; Fukumura, T.; Fujioka, H.; Ohno, H.; Koinuma, H.; Kawasaki, M. Modeling and Simulation of Polycrystalline ZnO Thin-Film Transistors. *J. Appl. Phys.* **2003**, *94*, 7768–7777.
34. Heo, Y. L.; Tien, L. C.; Norton, D. P.; Kang, B. S.; Ren, F.; Gila, B. P.; Pearton, J. Electrical Transport Properties of Single ZnO Nanorods. *Appl. Phys. Lett.* **2004**, *85*, 2002–2004.
35. Hong, W. K.; Sohn, J. I.; Hwang, D.-K.; Kwon, S.-S.; Jo, G.; Song, S.; Kim, S.-M.; Ko, H.-J.; Park, S.-J.; Welland, M. E.; *et al*. Tunable Electronic Transport Characteristics of Surface-Architecture-Controlled ZnO Nanowire Field Effect Transistors. *Nano Lett.* **2008**, *8*, 950–956.
36. Chen, H. Y.; Chen, R.-S.; Rajan, N. K.; Chang, F.-C.; Chen, L.-C.; Chen, K.-H.; Yang, Y.-J.; Reed, M. A. Size-Dependent Persistent Photocurrent and Surface Band Bending in M-Axial GaN Nanowires. *Phys. Rev. B* **2011**, *84*, 205443.
37. Chen, Y. L.; Yang, J. C.; Luo, C. W.; Laing, C. W.; Wu, K. H.; Lin, J.-Y.; Uen, T. M.; Juang, J. Y.; Chu, Y. H.; Kobayashi, T. Ultrafast Photoinduced Mechanical Strain in Epitaxial $BiFeO_3$ Thin Films. *Appl. Phys. Lett.* **2010**, *101*, 041902.
38. Corso, A. D.; Posternak, M.; Resta, R.; Baldereschi, A. Ab Initio Study of Piezoelectricity and Spontaneous Polarization in ZnO. *Phys. Rev. B* **1994**, *50*, 10715–10721.
39. Wang, H.-C.; Yang, C. C.; Feng, S.-W.; Zhang, B.-P.; Segawa, Y. Ultrafast Exciton Dynamics in a ZnO Thin Film. *Jpn. J. Appl. Phys.* **2009**, *48*, 022402.
40. Lee, S.; Apgar, B. A.; Martin, L. W. Strong Visible-Light Absorption and Hot-Carrier Injection in TiO_2/$SrRuO_3$ Heterostructures. *Adv. Energy Mater.* **2013**, *3*, 1084–1090.
41. Chen, M. W.; Chen, C. Y.; Lien, D. H.; Ding, Y.; He, J. H. Photoconductive Enhancement of Single ZnO Nanowire through Localized Schottky Effects. *Opt. Express* **2010**, *18*, 14836–14841.